

Recent Widespread Deceleration of Global Surface Urban Heat Islands Unveiled by Satellites

Wenfeng Zhan^{1, 2, 3}, Long Li^{1*}, TC Chakraborty⁴, Leiqiu Hu⁵, Dazhong Wang¹, Weilin Liao⁶, Shasha Wang¹, Huilin Du¹, Fan Huang¹, Chunli Wang¹, Zihan Liu¹, and Manchun Li⁷

¹Jiangsu Provincial Key Laboratory for Advanced Remote Sensing and Geographic Information Technology, International Institute for Earth System Science, Nanjing University, Nanjing, China

²Jiangsu Center for Collaborative Innovation in Geographical Information Resource Development and Application, Nanjing, China

³Frontiers Science Center for Critical Earth Material Cycling, Nanjing University, Nanjing, China

⁴Pacific Northwest National Laboratory, Richland, WA, USA

⁵Department of Atmospheric Science, University of Alabama in Huntsville, Huntsville, AL, USA

⁶Guangdong Key Laboratory for Urbanization and Geo-simulation, School of Geography and Planning, Sun Yat-sen University, Guangzhou, China

⁷School of Geography and Ocean Science, Nanjing University, Nanjing, China

*Corresponding author: L. Li (longlinju@gmail.com) at Nanjing University at Xianlin Campus, Nanjing, Jiangsu 210023, China

Contents of this file

Texts S1 to S7

Figures S1 to S24

Tables S1 to S2

References

A. Supplementary Texts

Text S1: City selection procedures and distribution across different climate zones

We consider all the world's urban clusters (cities, henceforth) with an urban area larger than 15 km² in 1990 and an urban area larger than 50 km² in 2018 in the present study. These two thresholds of urban area were chosen to filter the cities to ensure a larger sample of cities and an adequate number of pixels for statistics. The urban regions for 1990 and 2018 were considered, aiming to delineate global old urban area and newly urbanized area. By this filtering procedure, we obtained 2104 cities. According to the Köppen-Geiger climate classification (Kottek et al., 2006), these cities are distributed in arid (281 cities), equatorial (169 cities), polar (6 cities), snow (547 cities), and warm temperate climates (1101 cities).

Text S2: Descriptions of the datasets used in this study

We used satellite-derived data from multiple sources in our analysis. The datasets include land surface temperature (LST), land cover type, elevation, and urban boundary. Here we used the LST data (2000 – 2022) from the MODIS MOD11A1 product, consisting of daytime (~10:30) and nighttime (~22:30) observations with a spatial resolution of 1 km. The satellite LST data were used to quantify the surface urban heat island intensity (i.e., I_s) trends and the associated variabilities (i.e., A_i). We used the land cover type data for 2022 from the MODIS MCD12Q1 product, with a spatial resolution of 500 m using the IGBP classification scheme. The land cover type data were used to exclude pixels labeled as water bodies, wetlands, and permanent snow and ice in calculating the I_s and A_i . We considered the Shuttle Radar Topography Mission (SRTM) digital elevation model to eliminate the impacts from elevation changes in calculating the I_s and A_i , which is at 90 m resolution. We used the urban boundary data in 1990 and 2018 from Li et al. (2020), which were produced based on high-resolution (30 m) artificial impermeable surfaces. Such data were used to delineate urban areas (i.e., old urban area and newly urbanized area) and the associated rural surroundings required to estimate the I_s and A_i across global cities.

We further collected the normalized difference vegetation index (NDVI), albedo, aerosol optical depth (AOD), surface air temperature, precipitation, and population data to assist the attribution analysis of the A_i . We also collected impervious surface data to understand the urbanization impacts on A_i . Here we used the NDVI data (2000 – 2022) from the MODIS MOD13A2 product, with a spatial resolution of 1 km. We obtained the albedo data (2000 – 2022) from the MODIS MCD43A3 product at a spatial resolution of 500 m. The white-sky albedo product was used. We used the AOD data (2000 – 2022) from the MODIS MCD19A2 product, with a spatial resolution of 1 km. We used the surface air temperature and precipitation data (2000 – 2017) from the National Oceanic and Atmospheric Administration Physical Sciences Laboratory, with a spatial resolution of 0.5°. We used the population data (2000 – 2020) from the Global Human Settlement Layer at every 5-year intervals, with a spatial resolution of 1 km. We used impervious surface data (2000 – 2022) from Gong et al. (2020). During the satellite data collection process, we filtered out the data that was contaminated by clouds. In addition, these data were all resampled or aggregated to 1 km resolution and annual averages, mainly to examine the magnitude and drivers of the A_i across global cities.

Text S3: Selection of the urban boundary data

Urban boundary data produced based on different data resources have distinct characteristics. The Global Human Settlement Urban Centre Database (GHS-UCDB) data are generated primarily based on urban population and urban extent (Florczyk et al., 2019). The spatial extent of GHS-UCDB mainly describes the urban center and is therefore smaller than the physical built-up area. Nighttime light data is also commonly used for urban boundary extraction. However, this may ignore some areas with weak lighting and require thresholds to be set (Li & Zhou, 2017). Impervious surfaces can adequately characterize the spatial distribution of urban built-up areas. We therefore used the Global Urban Boundary (GUB) dataset based on impervious surfaces (Li et al., 2020). This helps to capture the contour of urban and rural fringes. In addition, the GUB data can enable rapid mapping and multi-temporal updating on a global scale. This significantly reduces the labor costs and subjectivity of defining urban boundaries for manual interpretation.

Text S4: Reliability assessment of the Terra MODIS LST data

We used the Aqua MODIS LST data to assess the reliability of Terra MODIS LST data. The results show that the Aqua and Terra MODIS LST data are relatively consistent in characterizing interannual I_s variability, showing the same fluctuation characteristics (Figure S16 in Supporting Information S1). In addition, the spatial patterns of A_l calculated based on Terra MODIS and Aqua MODIS LST data are similar (Figure S17 in Supporting Information S1). The correlation coefficient between the two was 0.78 ($p < 0.01$) during the daytime and 0.64 ($p < 0.01$) during the nighttime, showing a strong correlation (Figure S18 in Supporting Information S1). The difference between the two could be related to the difference in transit time and the influence of different degrees of clouds. Considering the reliability of Aqua satellite LST data (Good et al., 2022), the Terra MODIS LST data is therefore reliable in estimating I_s and A_l .

We further simulated the intra-day variations of LST for 2021 and 2022 using a diurnal temperature circle model with four intra-day Terra/Aqua MODIS LST observations to correct the Terra MODIS LST (Hong et al., 2021). The comparison of the pre- and post-correction LST data was used to evaluate the impact of the Terra satellite's orbital drift on the LST, I_s , and A_l estimates. The results show that the urban LST is underestimated by 0.642°C and 0.719°C in 2021 and 2022, respectively, and the rural LST is underestimated by 0.609°C and 0.684°C during the daytime, corresponding to an I_s underestimation of 0.033°C and 0.035°C; during the nighttime, the urban LST is overestimated by 0.153°C and 0.172°C in 2021 and 2022, respectively, and the rural LST were overestimated by 0.146°C and 0.165°C, and the corresponding I_s were overestimated by 0.007°C and 0.007°C, correspondingly (Figure S19 in Supporting Information S1). The orbital drift also biased the mean A_l of global 2104 cities from $-0.073^{\circ}\text{C}/\text{decade}^2$ (post-correction) to $-0.086^{\circ}\text{C}/\text{decade}^2$ (pre-correction) during the daytime, with an -15% bias, and from $-0.041^{\circ}\text{C}/\text{decade}^2$ (post-correction) to $-0.038^{\circ}\text{C}/\text{decade}^2$ (pre-correction) during the nighttime, with an 8% bias (Figure S20 in Supporting Information S1). Therefore, although the Terra satellite has undergone orbital drift, this does not alter the main findings. However, the errors may be further magnified as the orbital drift becomes larger, and thus this requires extra caution in the future.

Text S5: Reliability assessment of the calculation method of A_i

We compared the method that divided the entire study period into two periods and the method used in this study that distinguishes between multiple periods. The results show that the method used in this study (denoted as method 1) is strongly correlated with the method based on only two periods (denoted as method 2, treating I_s equally for each year) in estimating A_i , with correlation coefficients of 0.88 ($p < 0.01$) and 0.89 ($p < 0.01$) in daytime and nighttime, respectively, and the slope of the fit approximates to a 1:1 line (Figure S21 in Supporting Information S1). This implies that the method in this study is effective and could accurately estimate A_i .

Text S6: Spatial pattern of contributions from $A_{\delta NDVI}$ and $A_{\delta Albedo}$ to A_i

We quantified the respective contributions (measured in $^{\circ}\text{C}/\text{decade}^2$) of the $A_{\delta NDVI}$ and $A_{\delta Albedo}$ to the observed A_i during the day and at night (Figure S15 in Supporting Information S1), as these two factors are the most important drivers of the A_i . Our results reveal significant spatial and diurnal differences in their impacts on the A_i . Spatially, the $A_{\delta NDVI}$ -led contribution is relatively larger in East Asia and Africa, possibly due to the larger increase in $\delta NDVI$ trends over these regions (Figure S22 in Supporting Information S1). The $A_{\delta Albedo}$ -led contribution is greater in mid- and high-latitude cities in the Northern Hemisphere, which may be related to the stronger regional albedo-climate feedback (Betts, 2000; Lee et al., 2011). Diurnally, the $A_{\delta Albedo}$ -led contribution is slightly larger at night than during the day, while the $A_{\delta NDVI}$ -led contribution is considerably higher during the day. This is mostly because vegetation strongly modulates I_s during daytime through evaporative cooling (Chakraborty & Lee, 2019), while the impact of albedo is associated with changes in heat storage during daytime that can carry over to impact I_s at night (Zhao et al. 2014). With respect to different urbanization subclasses, the $A_{\delta NDVI}$ - and $A_{\delta Albedo}$ -led contributions are greater in the old urban area than in the newly urbanized area (Figure S23 in Supporting Information S1). This explains the faster I_s deceleration in the old urban area than in the newly urbanized area due to their dominant role in promoting I_s deceleration.

Text S7: Limitations of this study

We acknowledge five limitations in this study. First, our analysis covers only the past two decades due to the availability of high-quality satellite LST data. Landsat and NOAA satellites provide LST data with longer records, but they are restricted in accurately estimating I_s trend (V_i) due to orbital drift (for NOAA-AVHRR; Gutman, 1999) or long revisiting periods (for Landsat-series; Zhou et al., 2019). Currently, LST data acquired by MODIS represent the sole reliable and robust data source for investigating A_i at a fine resolution over cities worldwide. One may still question whether two decades are enough to detect robust shifts in V_i . We argue that these detected shifts should be reliable because they are mainly driven by noteworthy changes in surface properties during urbanization over this period. Nevertheless, we acknowledge the necessity for investigating shifts in V_i over longer periods, but this requires the generation of high-quality global LST products with high spatial resolutions. Second, investigating higher-order derivatives is relatively difficult due to the discreteness of satellite data and the influence of weather conditions, land cover change and data noise. We conducted two trend calculations to derive A_i (i.e., second-order signal) based on the approximate form of the second-order difference, with relatively longer step length than unit step length. This can effectively eliminate the impacts of inter-annual I_s fluctuations on the A_i estimation, providing an average A_i over the entire period. Nevertheless, we acknowledge that the

degree of difficulty faced is likely to be further exacerbated and may even become less feasible when one goes further into the investigation of higher-order change features, such as third-order signals. Third, our study mainly focuses on surface UHI, while canopy UHI based on air temperature is more closely related to heat stress (Chakraborty et al., 2022). Future endeavors could delve into UHI trends based on air temperature and thermal comfort indices, which further incorporate humidity, wind speed, and radiant temperature (Middel et al., 2021). Nevertheless, efforts remain required to develop advanced and reliable algorithms for obtaining long-term pixel-based air temperatures and thermal comfort index values across each individual city worldwide. Fourth, satellite LST data used to estimate I_s are clear-sky observations, which can lead to biases in the I_s estimates (Yang et al., 2024). Consequently, this may also distort the magnitude of the I_s acceleration or deceleration. Regarding this issue, we collected the gap-filled MODIS LST data provided by Zhang et al., (2022) to investigate the influence of cloud contamination on our findings by comparing the A_i estimated by observed MODIS LST and gap-filled MODIS LST. The results show that the A_i calculated based on Aqua MODIS data is strongly correlated with the outcomes based on gap-filled MODIS LST (Figure S24 in Supporting Information S1). Therefore, despite the influence of cloud contamination on satellite observations, this should not affect our main findings (e.g., widespread I_s deceleration). Nevertheless, a reliable all-sky LST dataset is still essential to understand the temporal dynamics of I_s . Lastly, a data-driven approach was employed to elucidate the relationships between A_i and its drivers. This approach can offer explanations for the A_i , but providing correlations rather than causality. We acknowledge that our approach simplifies the complexity of impacts of urbanization and climate change on A_i . Physics-based attribution methods may offer more precise interpretations of the A_i .

B. Supplementary Figures

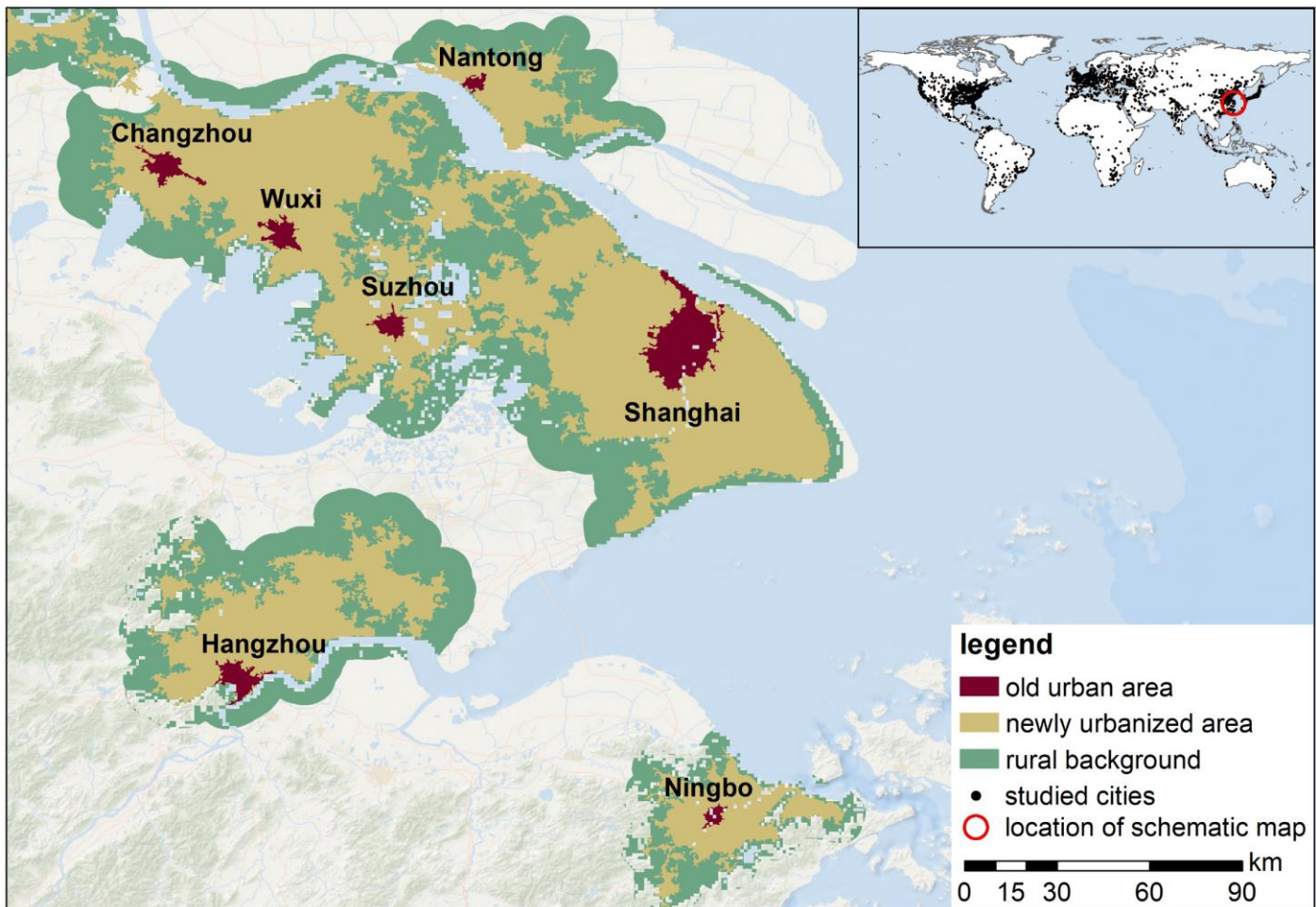


Figure S1. Schematic for delineating old urban area, newly urbanized area, and rural background over a typical urban agglomeration in China. Old urban area is defined as the urban surfaces demarcated by the 1990 urban boundary; newly urbanized area comprises of the urban surfaces located between the 1990 and 2018 urban boundaries; and rural background is defined as the 1.5 times buffer of the urban area situated outside the 2018 urban boundary. The pixels labeled as water bodies, wetlands, and permanent snow and ice and the rural pixels with an elevation exceeding ± 50 m above the mean urban elevation were excluded to eliminate their influence on the estimation of I_s .

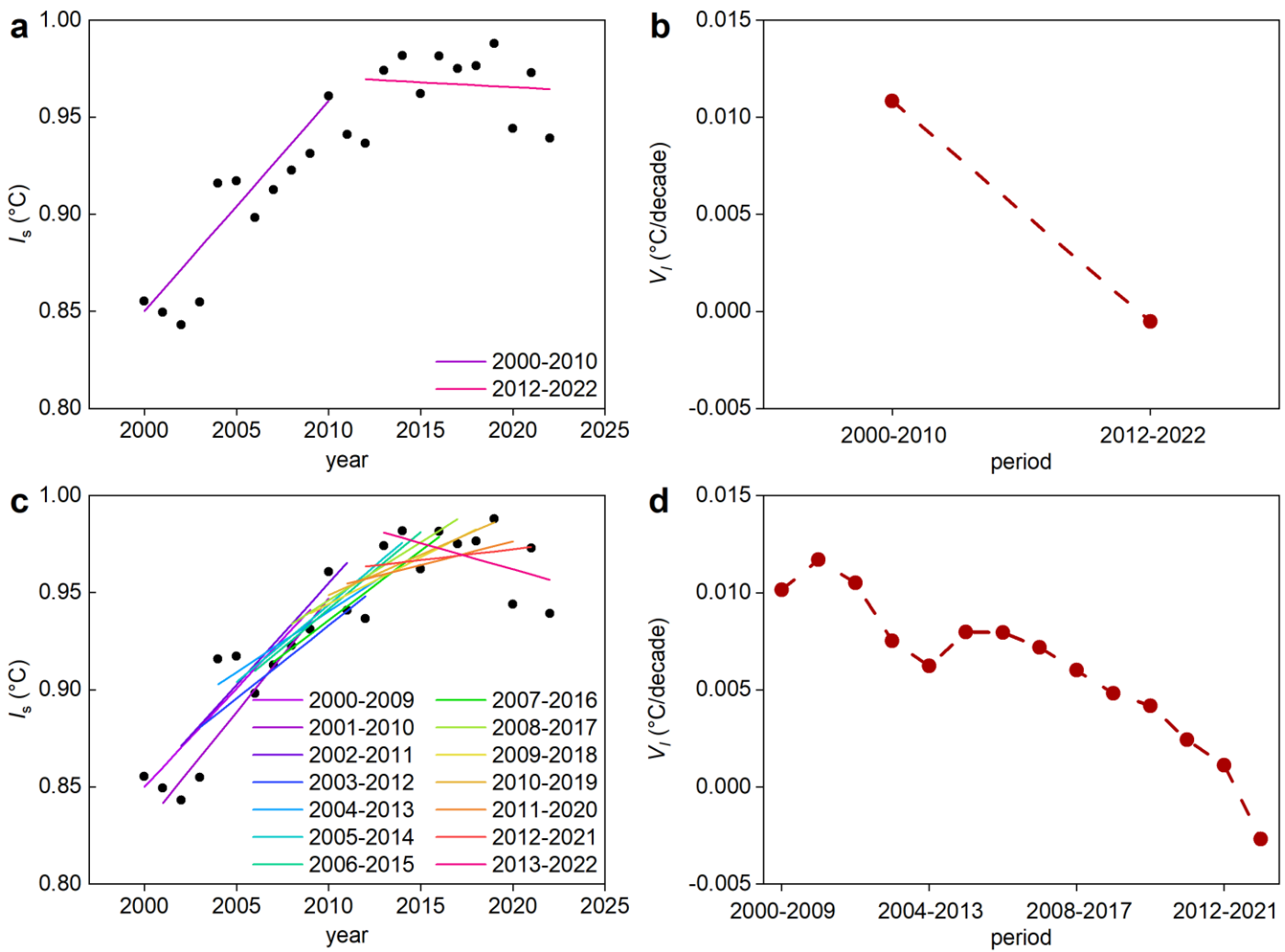


Figure S2. Schematics showing the comparison of A_I estimated by methods based on two periods (change rate of V_I between 2000-2010 and 2012-2022) and multiple periods (this study). (a) Linear fitting for two periods; (b) V_I for two periods; (c) linear fitting for multiple periods; and (d) V_I for multiple periods.

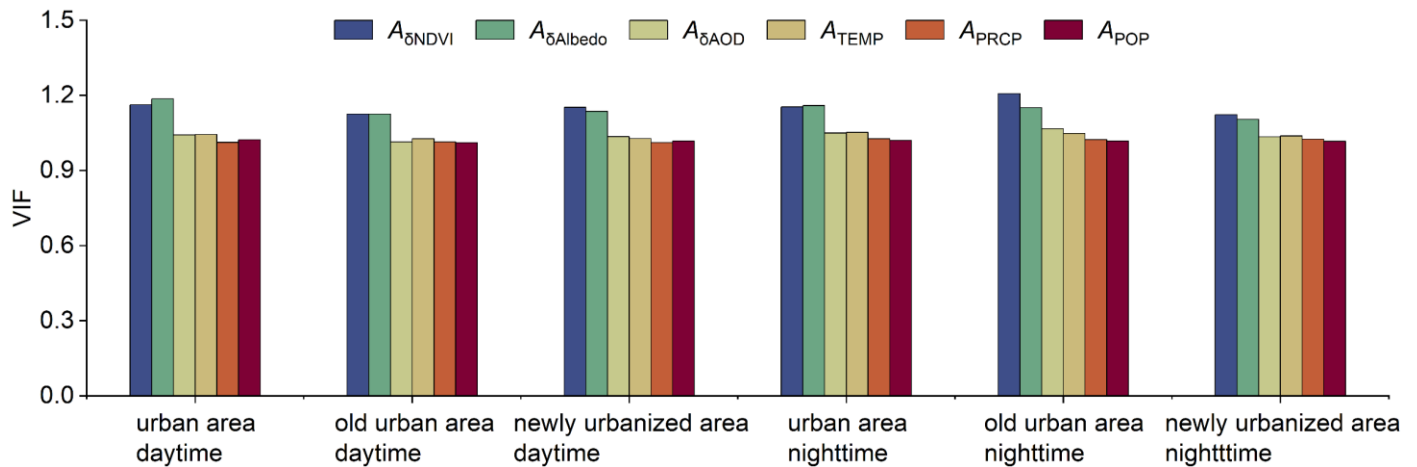


Figure S3. Variance inflation factor (VIF) of the explanatory variables for the A_i . The grouped bar charts (i.e., urban subdivisions and daytime/nighttime) indicate the VIF of explanatory variables for the A_i under different categories. $A_{\delta NDVI}$, $A_{\delta Albedo}$, and $A_{\delta AOD}$ denote the second derivatives of the changes in urban-rural differences for normalized difference vegetation index (NDVI), albedo, and aerosol optical depth (AOD), and A_{TEMP} , A_{PRCP} , and A_{POP} denote the second derivatives of the changes in rural surface air temperature (TEMP), precipitation (PRCP), and urban population (POP).

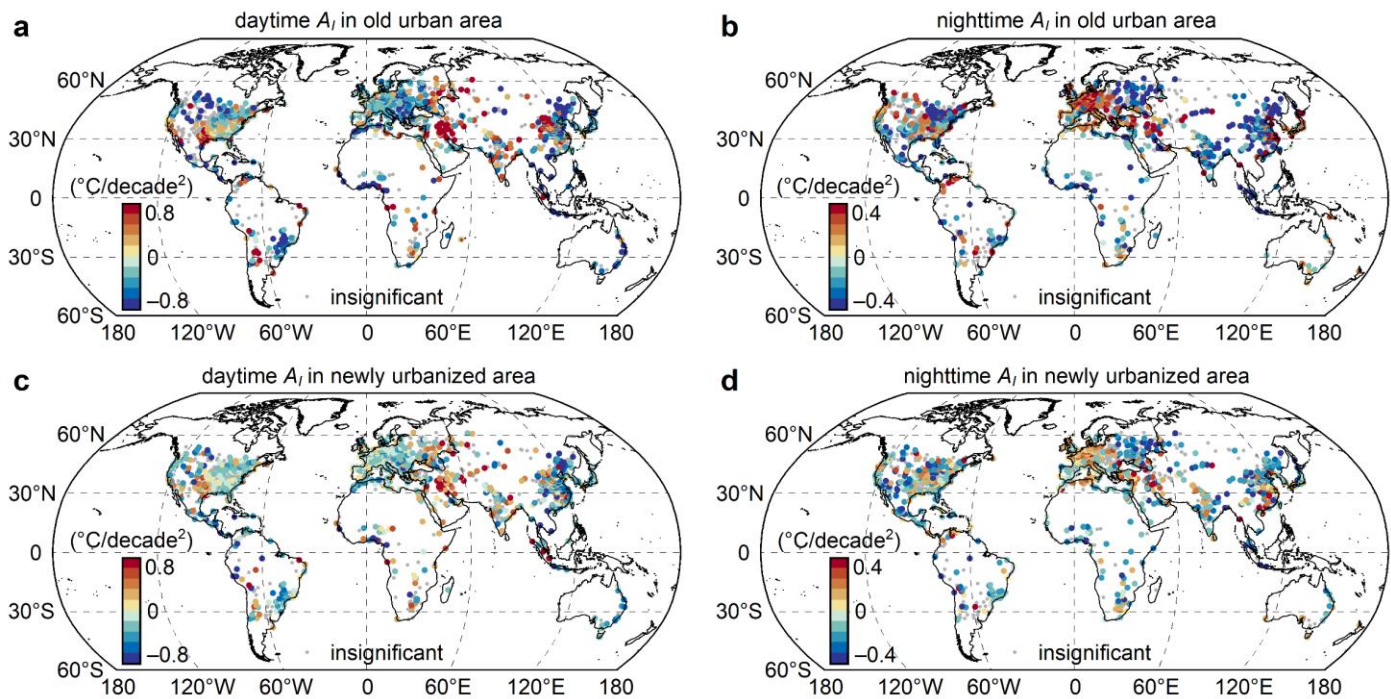


Figure S4. Spatial pattern of A_i in old urban area and newly urbanized area over 2104 cities worldwide for 2000-2022. Spatial pattern of A_i in old urban area (a) and newly urbanized area (c) during the day. (b), (d), as in (a), (c), but showing nighttime results corresponding to panels a and c, respectively.

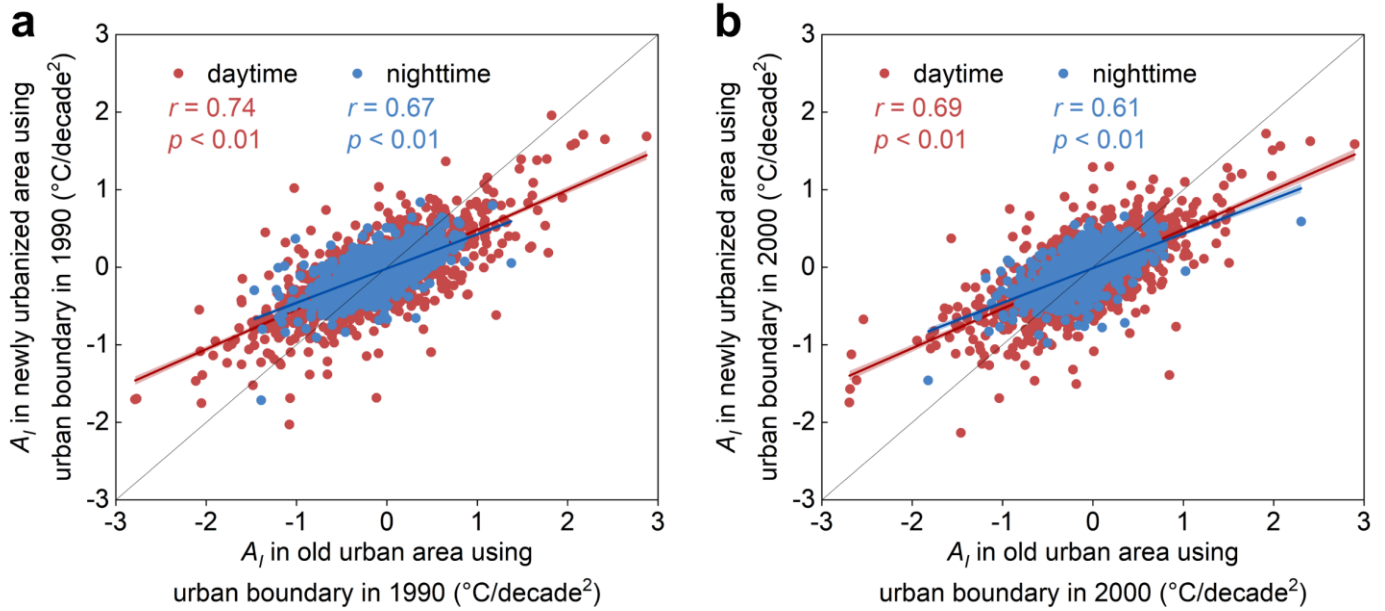


Figure S5. The relationship between A_l in old urban area and newly urbanized area over 2104 cities worldwide during the day and night. Comparison of A_l in old urban area and newly urbanized area using urban boundary in 1990 (a) and 2000 (b). The red and blue backgrounds indicate 95% confidence interval of the linear fit. Note that in this study, the urban boundary in 1990 was primarily used to delineate the old urban area and newly urbanized area, while the urban boundary in 2000 was used to assess the impact of year selection of urban boundaries on the correlation of A_l between old urban area and newly urbanized area.

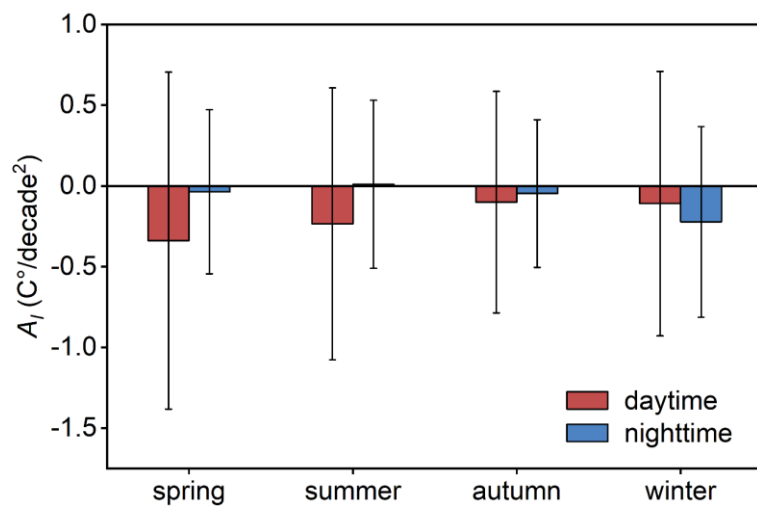


Figure S6. Seasonal variations in A_i across global cities with significant A_i for 2000-2022.

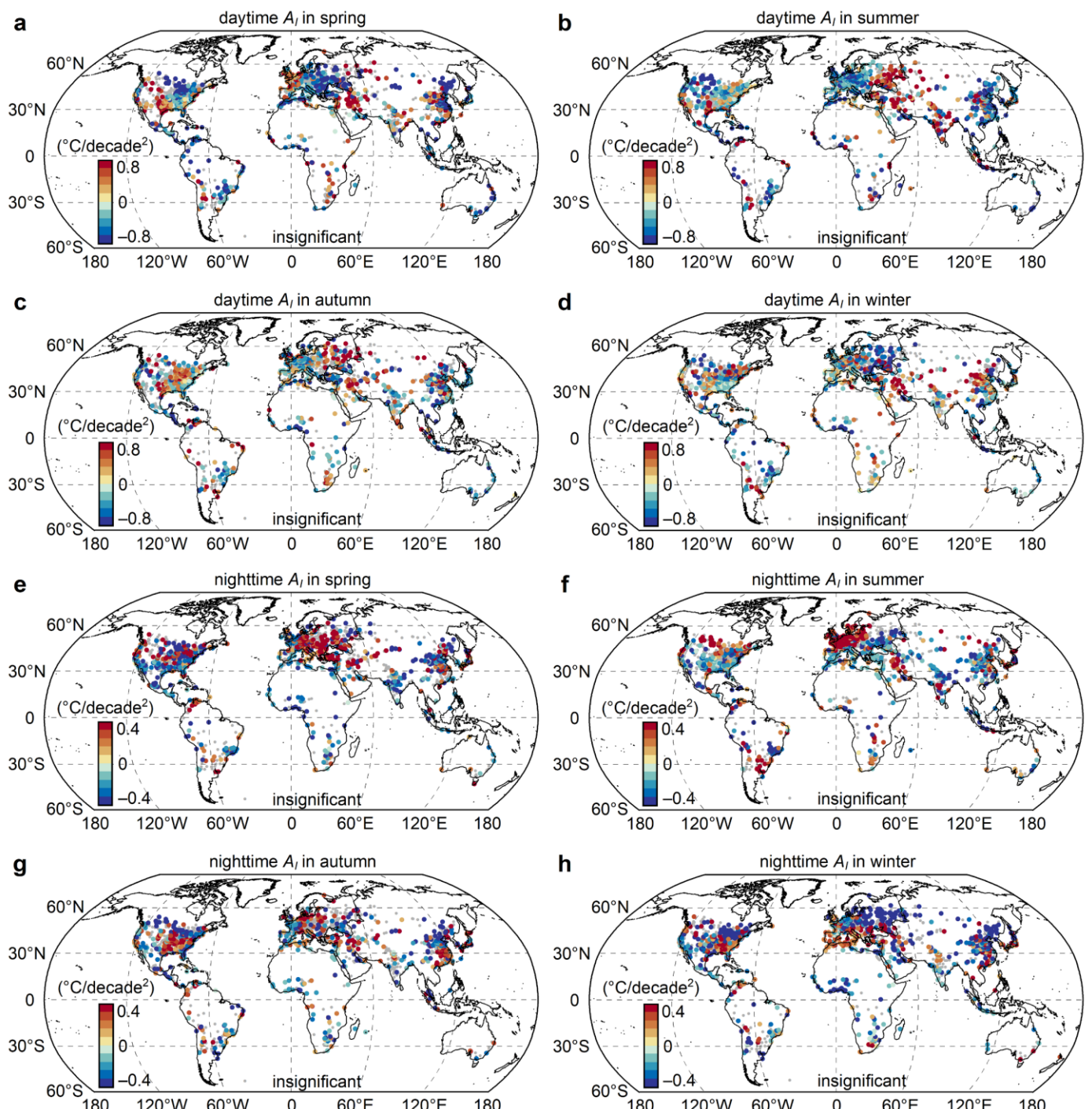


Figure S7. Spatial pattern of seasonal variations in A_i across global cities for 2000-2022. (a) Daytime A_i in spring; (b) daytime A_i in summer; (c) daytime A_i in autumn; and (d) daytime A_i in winter. (e)-(h), as in (a)-(d), but showing nighttime results corresponding to panels a-d, respectively.

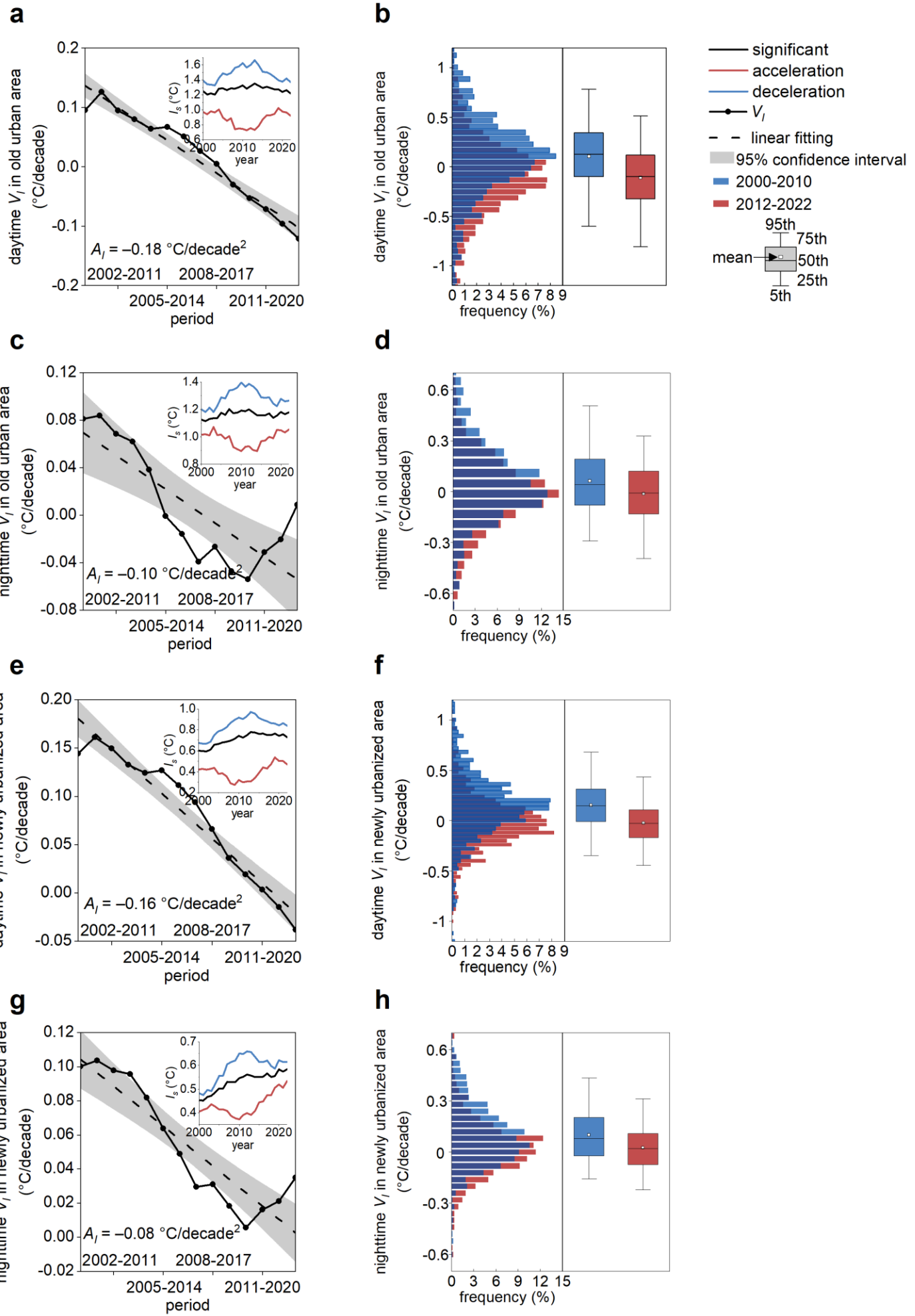


Figure S8. Temporal variations in I_s , and V_l , and the A_l in old urban area and newly urbanized area over all cities with significant A_l . Temporal variations in I_s , and V_l and the A_l in old urban area during the day (a). The left panel shows the frequency distributions of daytime V_l in old urban area across these cities between 2000-2010 and 2012-2022, while the right panel shows the boxplots of daytime V_l in old urban area during these two periods (b). (c) to (h), as in (a), (b), but showing different cases (e.g., during the day or night, and in old urban area or newly urbanized area). In (a), (c), (e), and (g), for different cases, the red solid lines indicate the mean I_s variations; the red dot-dash lines indicate the I_s variations for all cities with $A_l > 0$; the red dotted lines indicate the I_s variations for all cities with $A_l < 0$; the black solid lines indicate the variations in the V_l ; the black dotted lines indicate the linear fit of the V_l (with the slope denoting the A_l); and the gray backgrounds indicate 95% confidence interval of the linear fit.

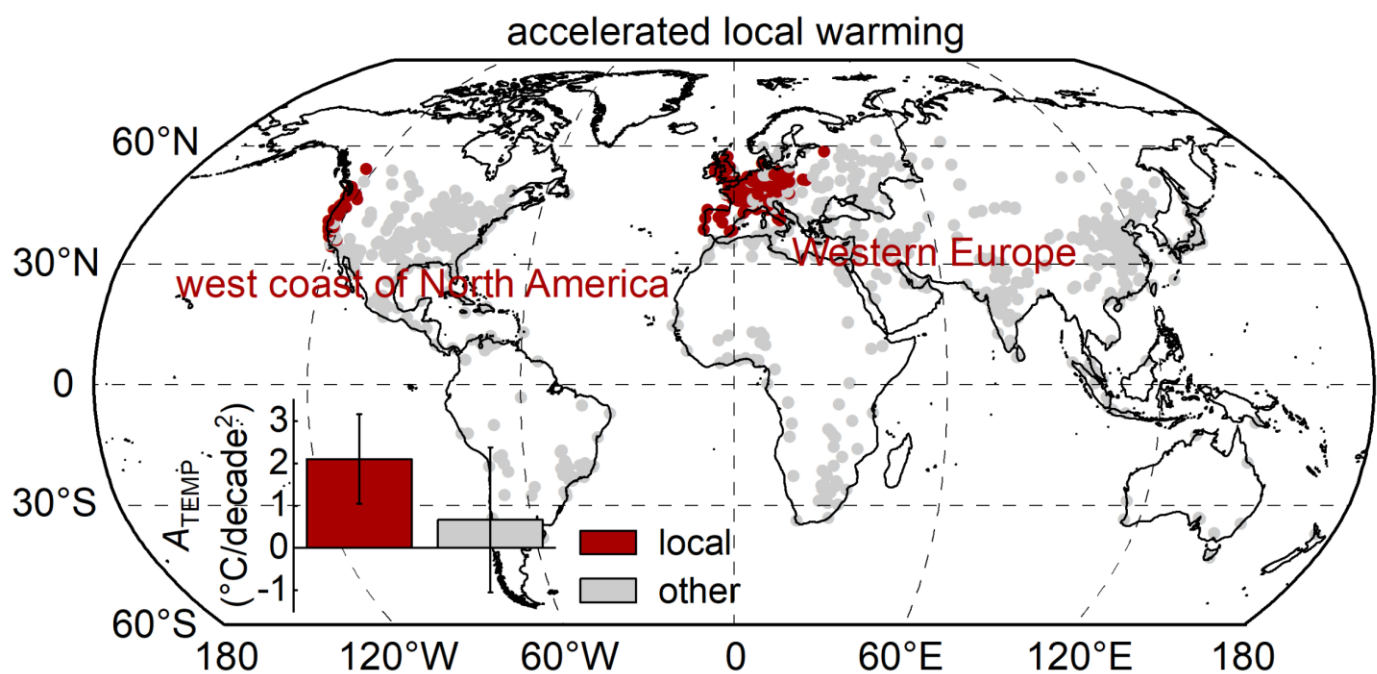


Figure S9. Comparison of the variabilities of the trends of the surface air temperature (A_{TEMP}) among local and other cities. The local cities represent those of west coast of Western Europe and North America and with A_t dominated by A_{TEMP} . The other cities indicate the cities examined in this study except the local cities.

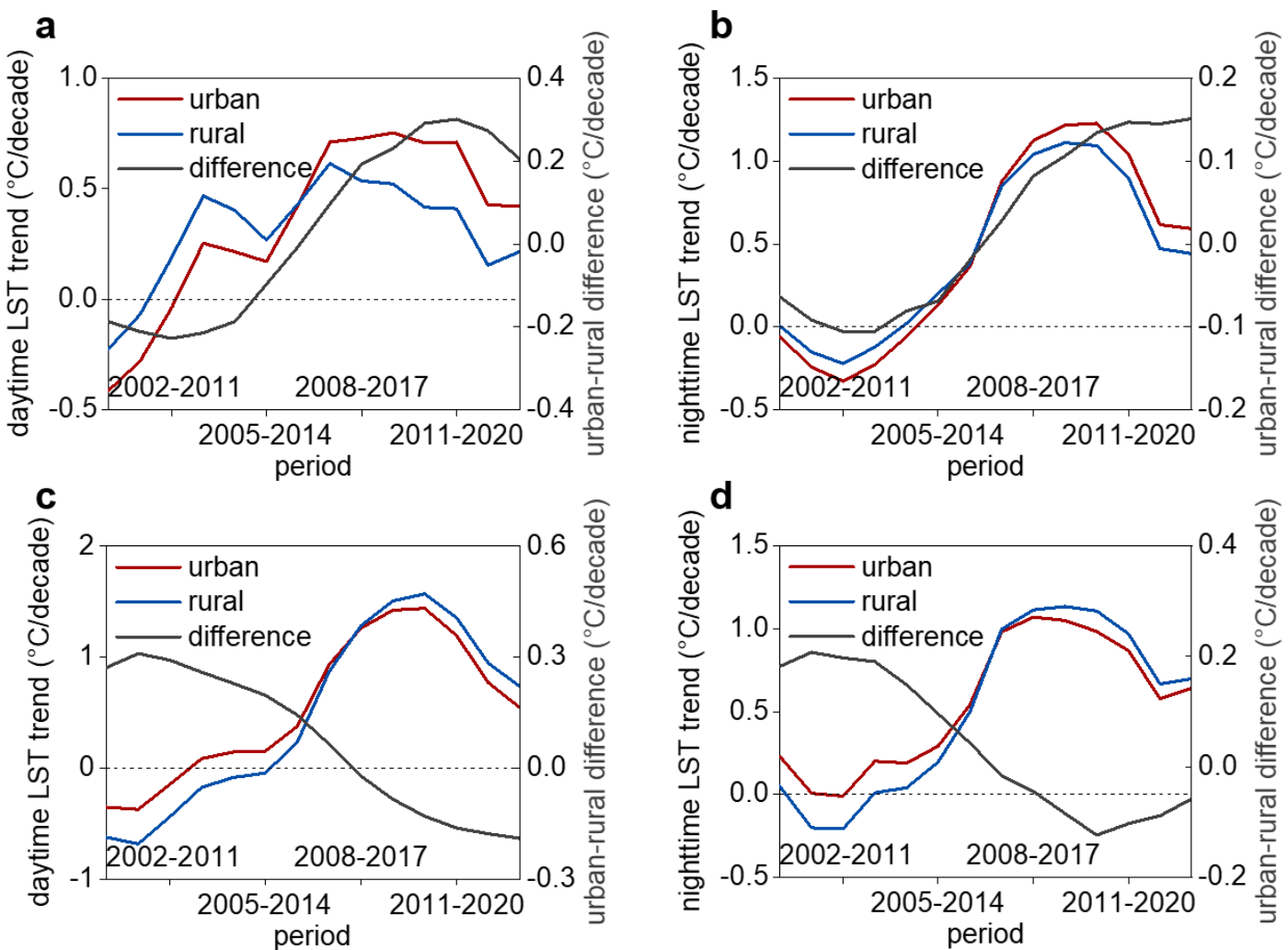


Figure S10. Urban/rural LST trends as well as their difference (i.e., V_i) over all cities with significant A_i for 2000-2022. (a) Daytime LST trends and their difference over all cities with positive A_i ; (b) nighttime LST trends and their difference over all cities with positive A_i ; (c) daytime LST trends and their difference over all cities with negative A_i ; and (d) nighttime LST trends and their difference over all cities with negative A_i .

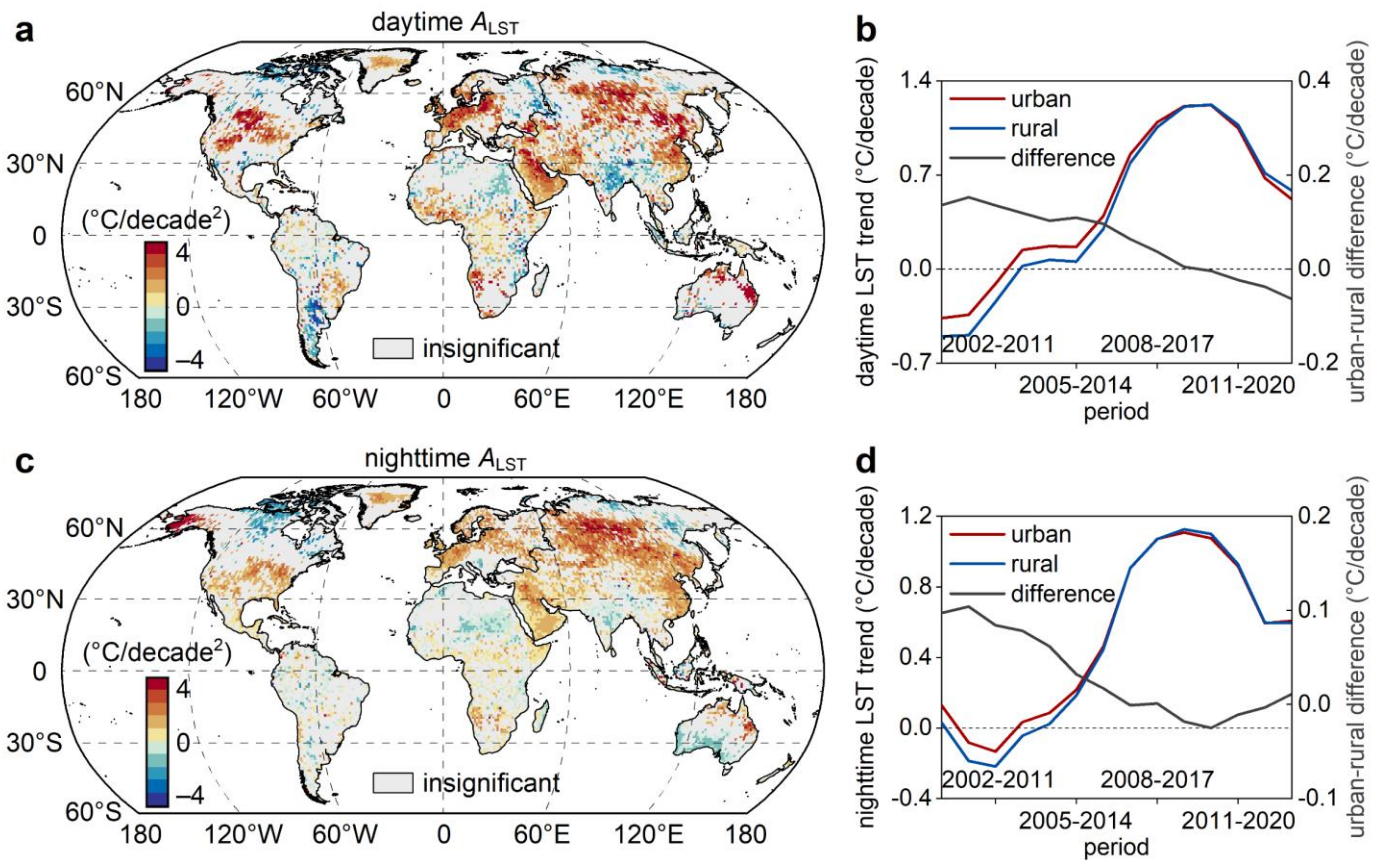


Figure S11. Global LST acceleration (A_{LST}) and urban/rural LST trends as well as their difference (i.e., V_i) over all cities with significant A_i for 2000–2022. (a) Daytime A_{LST} ; and (b) urban and rural LST trends across multiple periods. (c), (d), as in (a), (b), but showing nighttime results corresponding to panels a and b, respectively.

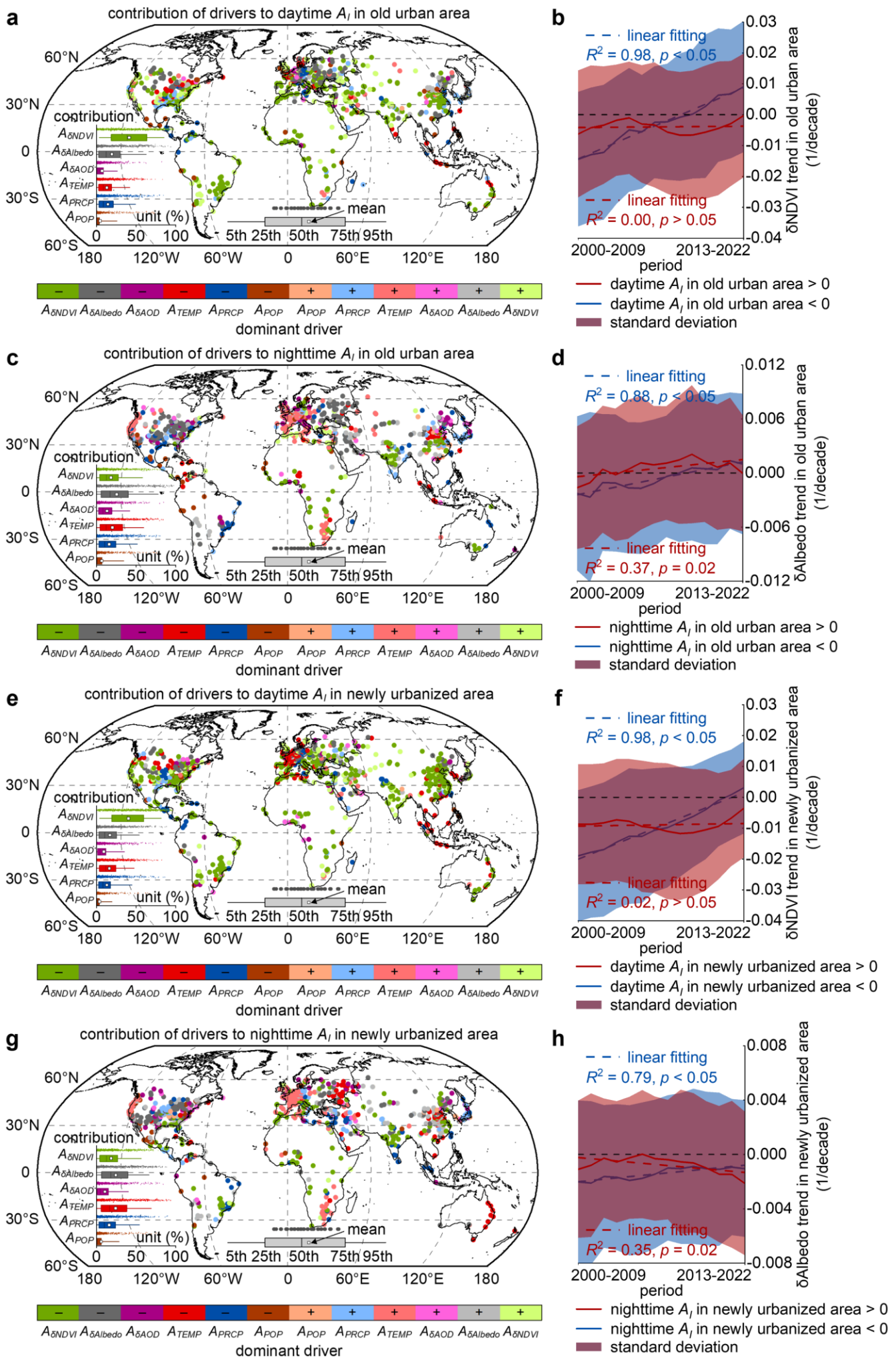


Figure S12. Dominant drivers of A_I in old urban area and newly urbanized area across global cities. The most dominant drivers of A_I and their percentage contributions in old urban area for each city during the day (a). Temporal variations of the urban-rural normalized difference vegetation index (NDVI) difference (δNDVI) for city categories with $A_I > 0$ and with $A_I < 0$ in old urban area during the day (b). (c) to (h), as in (a), (b), but showing different cases (e.g., during the day or night, in old urban area or newly urbanized area, and for δNDVI trend or urban-rural albedo difference (δAlbedo) trend). In panels a, c, e, and g, the '+' indicates a positive contribution to A_I , while '-' indicates a negative contribution. $A_{\delta\text{NDVI}}$, $A_{\delta\text{Albedo}}$, and $A_{\delta\text{AOD}}$ denote the second derivatives of the changes in urban-rural differences for NDVI, albedo, and aerosol optical depth (AOD), and A_{TEMP} , A_{PRCP} , and A_{POP} denote the second derivatives of the changes in rural surface air temperature (TEMP), precipitation (PRCP), and urban population (POP).

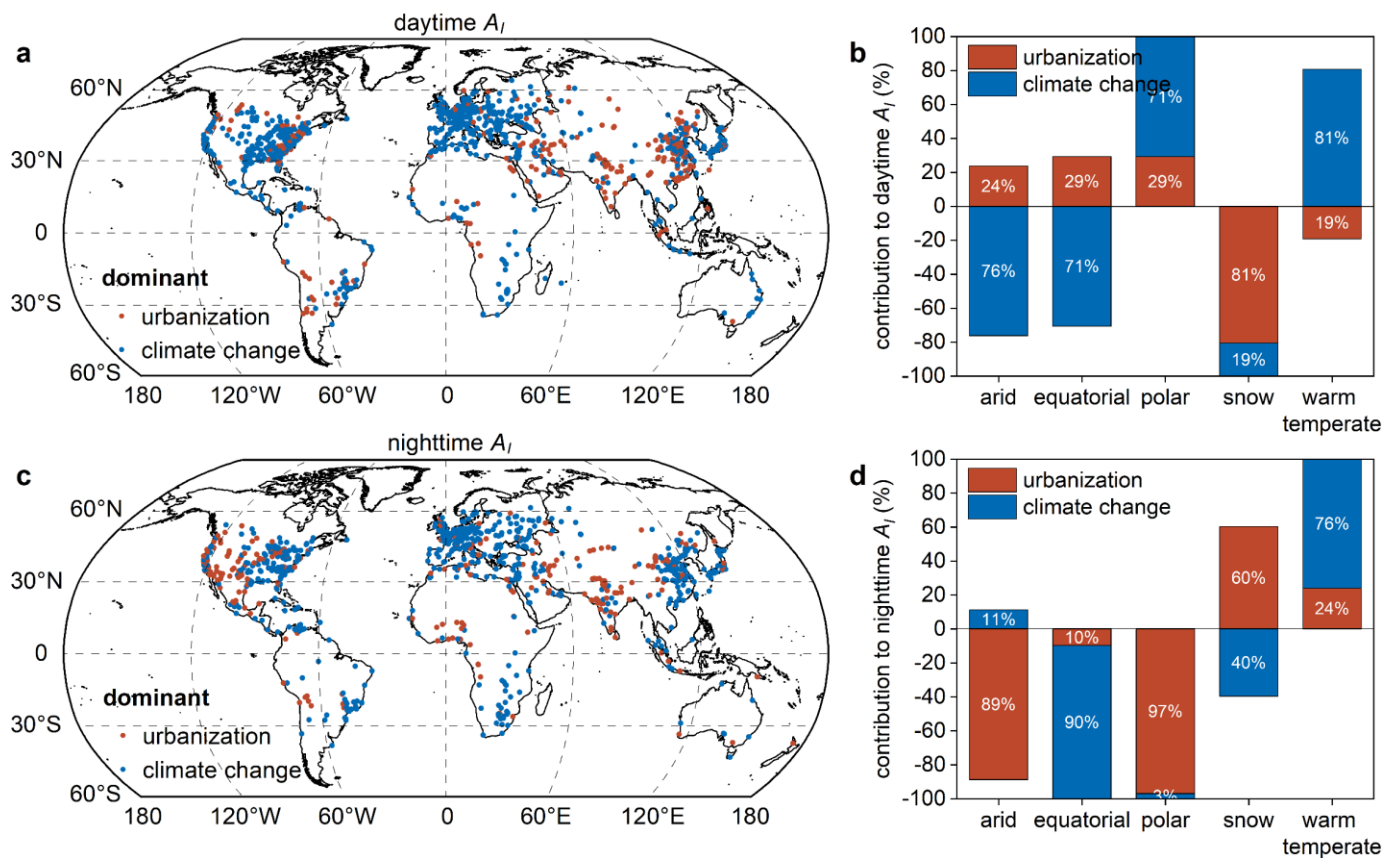


Figure S13. The dominant drivers of A_t and the relative contributions of urbanization and climate change to A_t . The dominant drivers of A_t during daytime (a) and nighttime (c) across global cities. The relative contributions of urbanization and climate change to A_t during daytime (b) and nighttime (d) across climate zones.

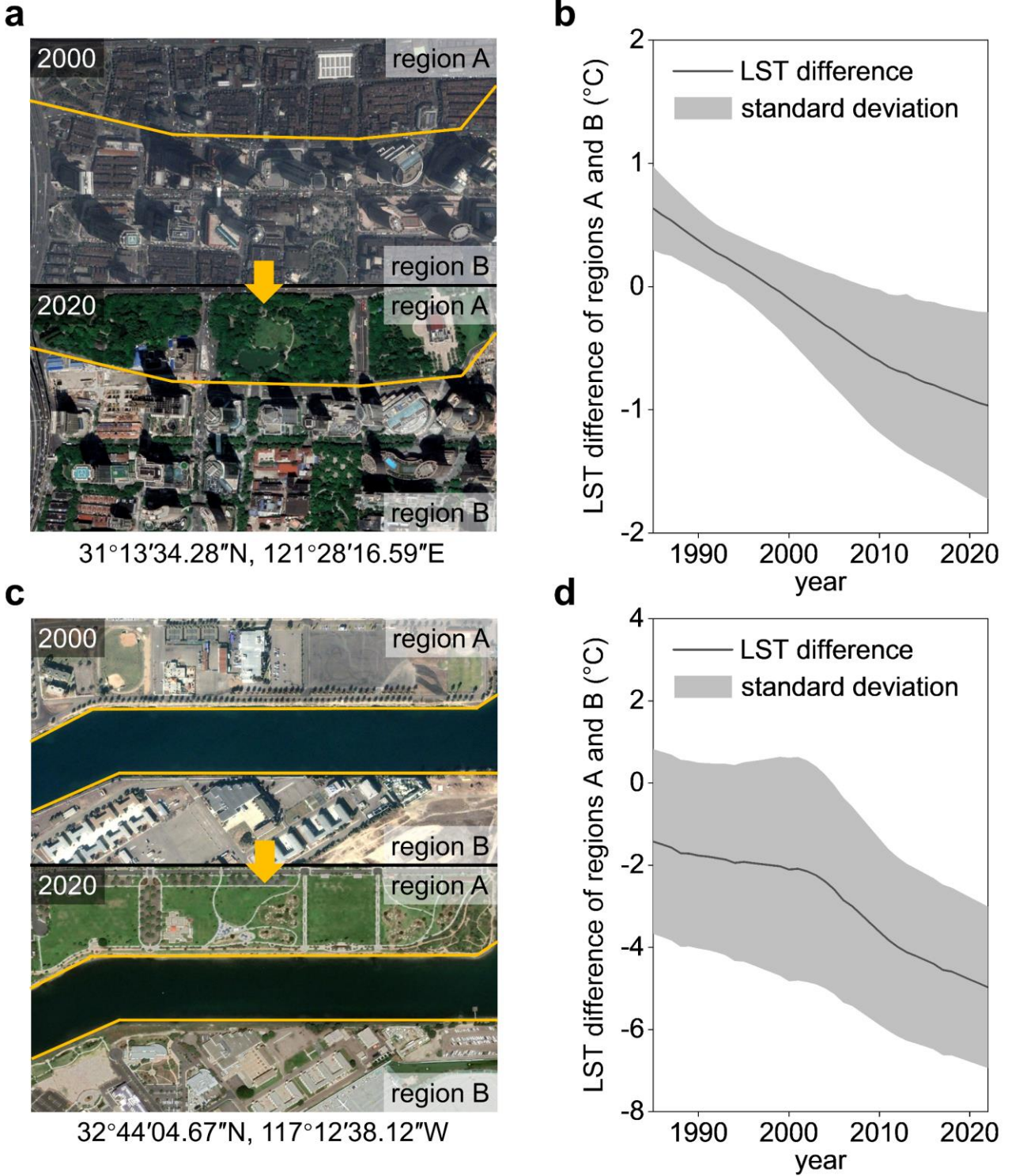


Figure S14. The impacts of urban renewal on land surface temperature (LST). The types of urban land cover changes in Shanghai, China (a) and San Diego, USA (c) from 2000 to 2020, including region A (urban renewal, namely impervious surface converted to parkland) and region B (control/reference regions, namely relatively stable impervious surface). The LST differences of regions A and B in Shanghai, China (b) and San Diego, USA (d) reflect the impacts of urban renewal on LST. The LST data used here were obtained by reconstructing the Landsat LST from 1985 to 2022 at a resolution of 120m based on the previously adopted method (Li et al., 2022).

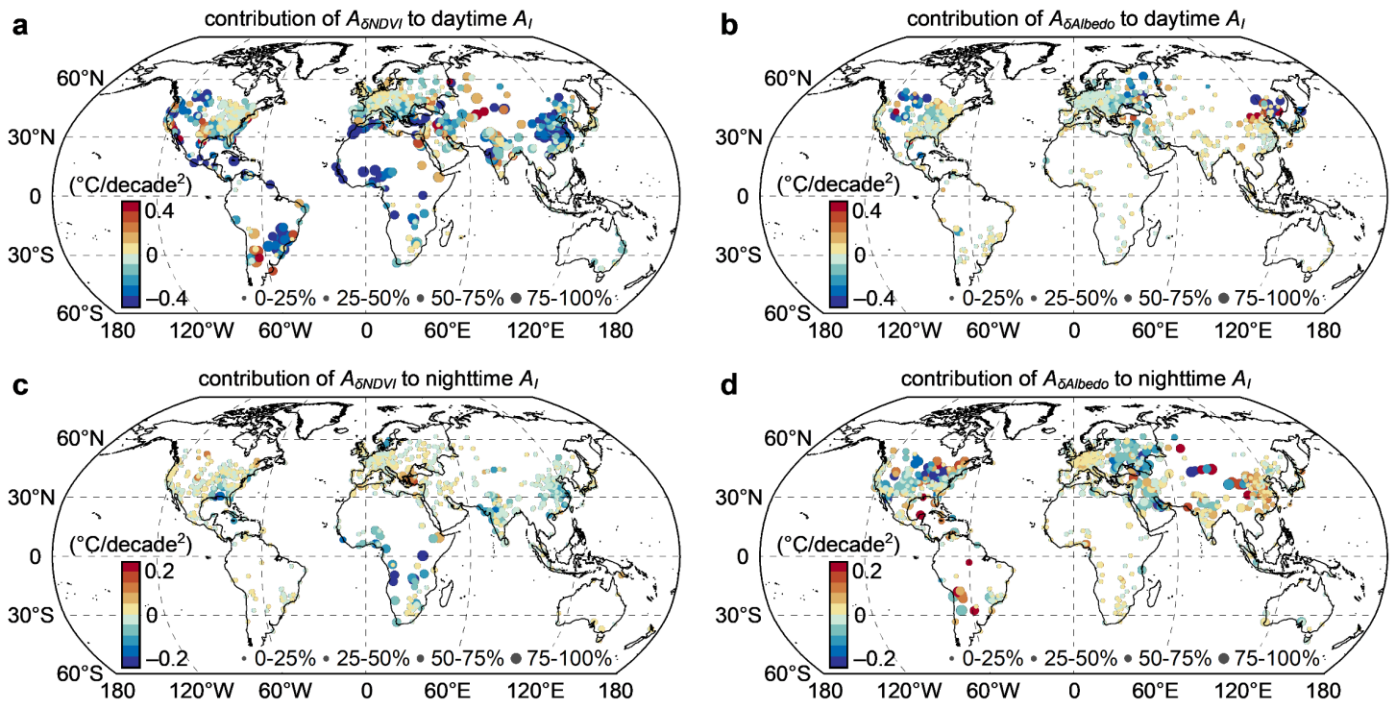


Figure S15. Contributions from the variabilities of the trends of the urban-rural normalized difference vegetation index (NDVI) and albedo differences (the $A_{\delta NDVI}$ and $A_{\delta Albedo}$) to the A_I across global cities. Contributions from the $A_{\delta NDVI}$ (a) and $A_{\delta Albedo}$ (b) to the A_I during the day. (c), (d), as in (a), (b), but showing nighttime results corresponding to panels a and b, respectively. The color and size of the circles signify the value and percentage of contribution from the $A_{\delta NDVI}$ and $A_{\delta Albedo}$ to the A_I .

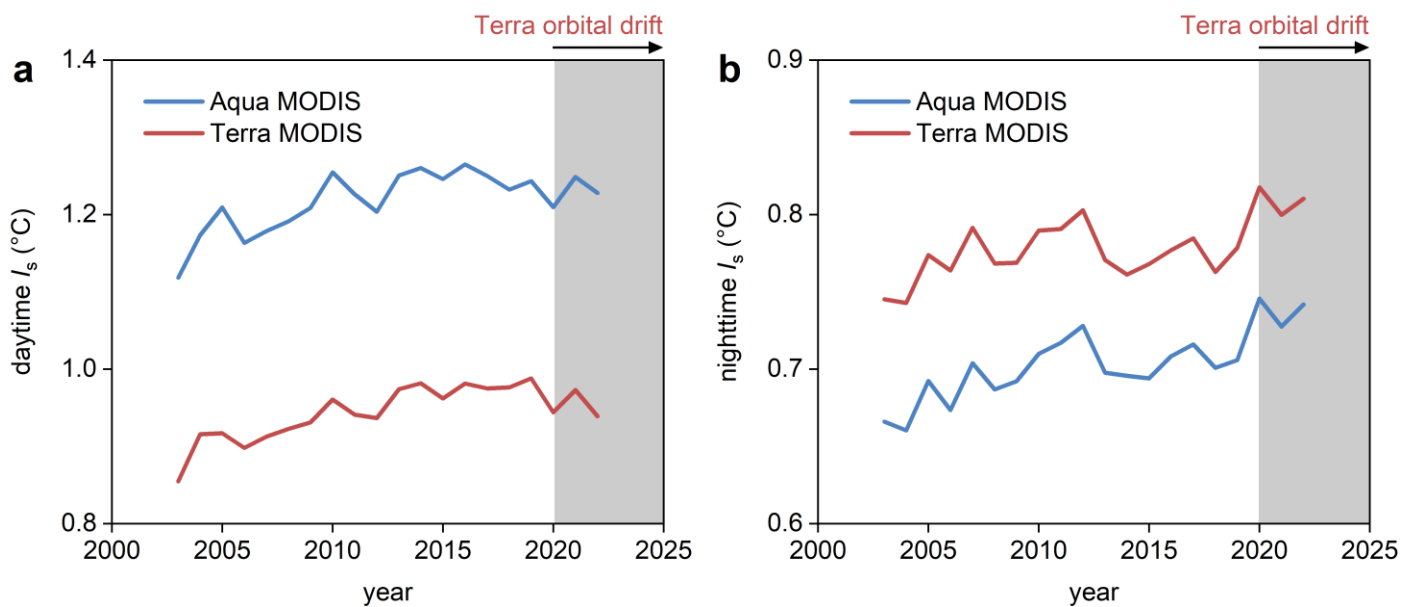


Figure S16. Interannual variations in I_s based on Aqua and Terra MODIS LST observations. (a) Daytime comparison; and (b) nighttime comparison.

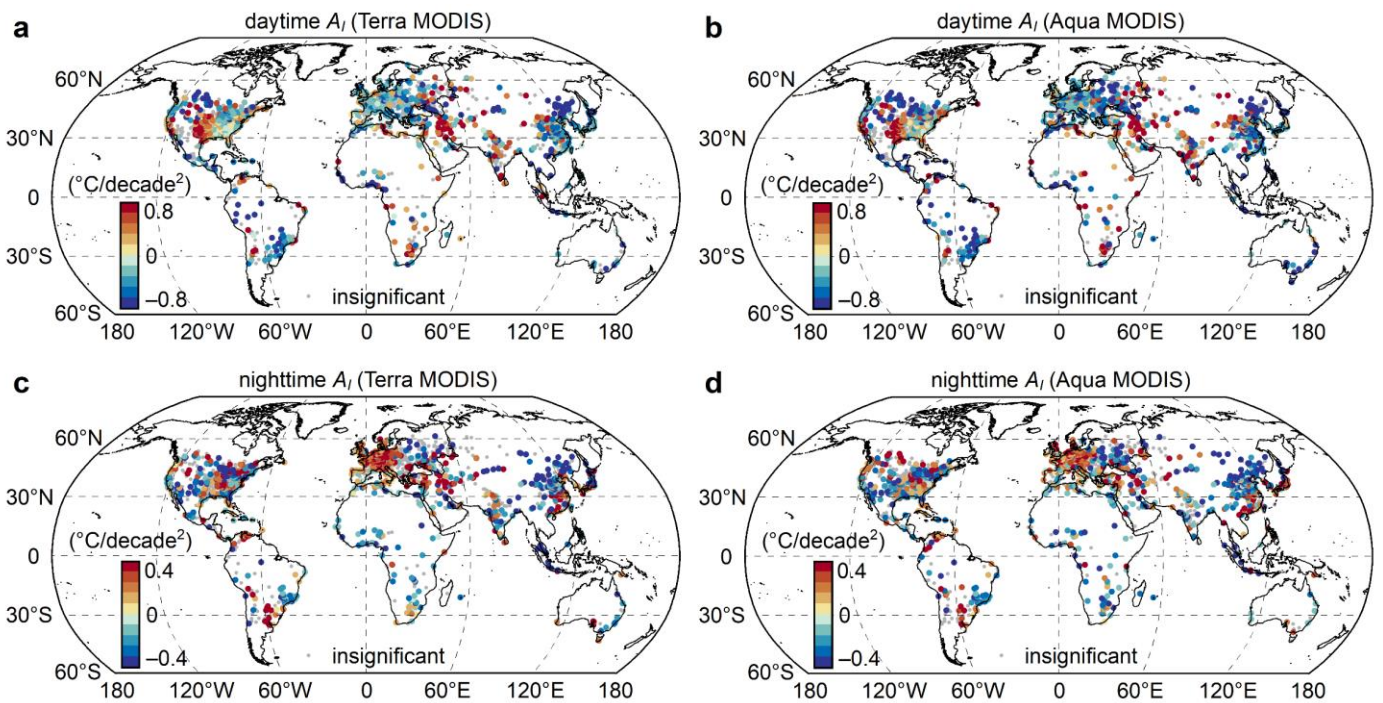


Figure S17. Spatial pattern of A_i estimated by Terra and Aqua MODIS data over 2104 cities worldwide for 2003-2022. (a) Terra-derived daytime A_i ; (b) Aqua-derived daytime A_i ; (c) Terra-derived nighttime A_i ; and (d) Aqua-derived nighttime A_i .

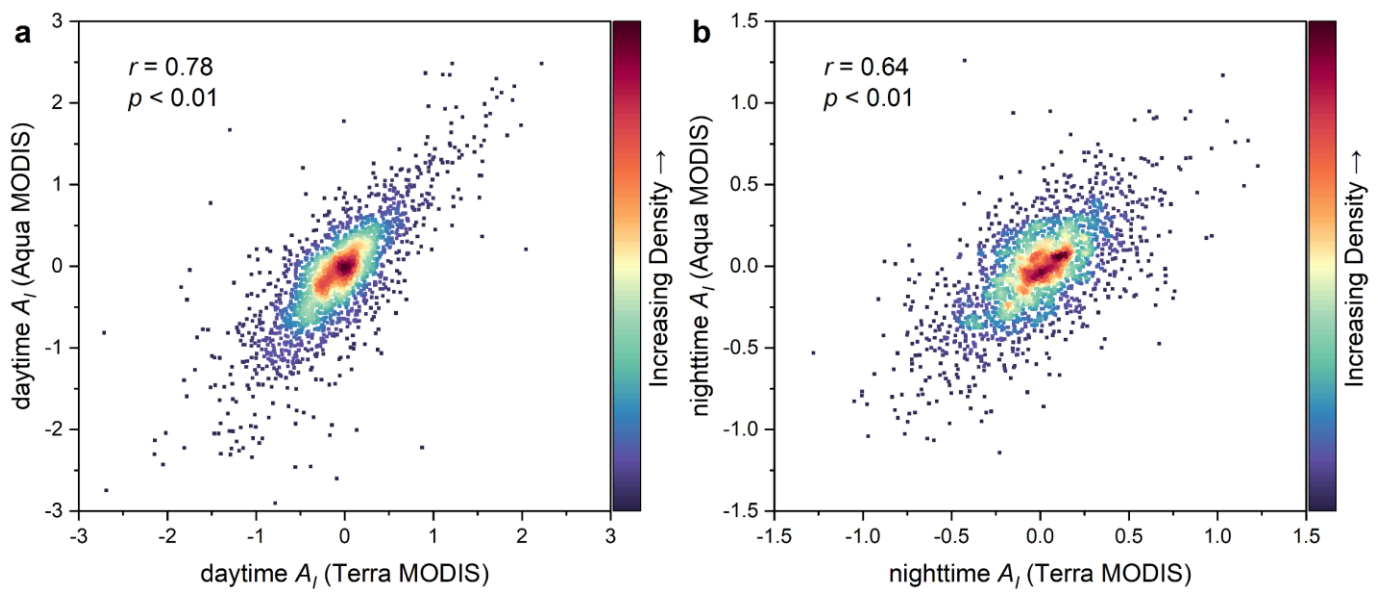


Figure S18. Correlation of A_t estimated by Terra and Aqua MODIS data. (a) Daytime comparison; and (b) nighttime comparison.

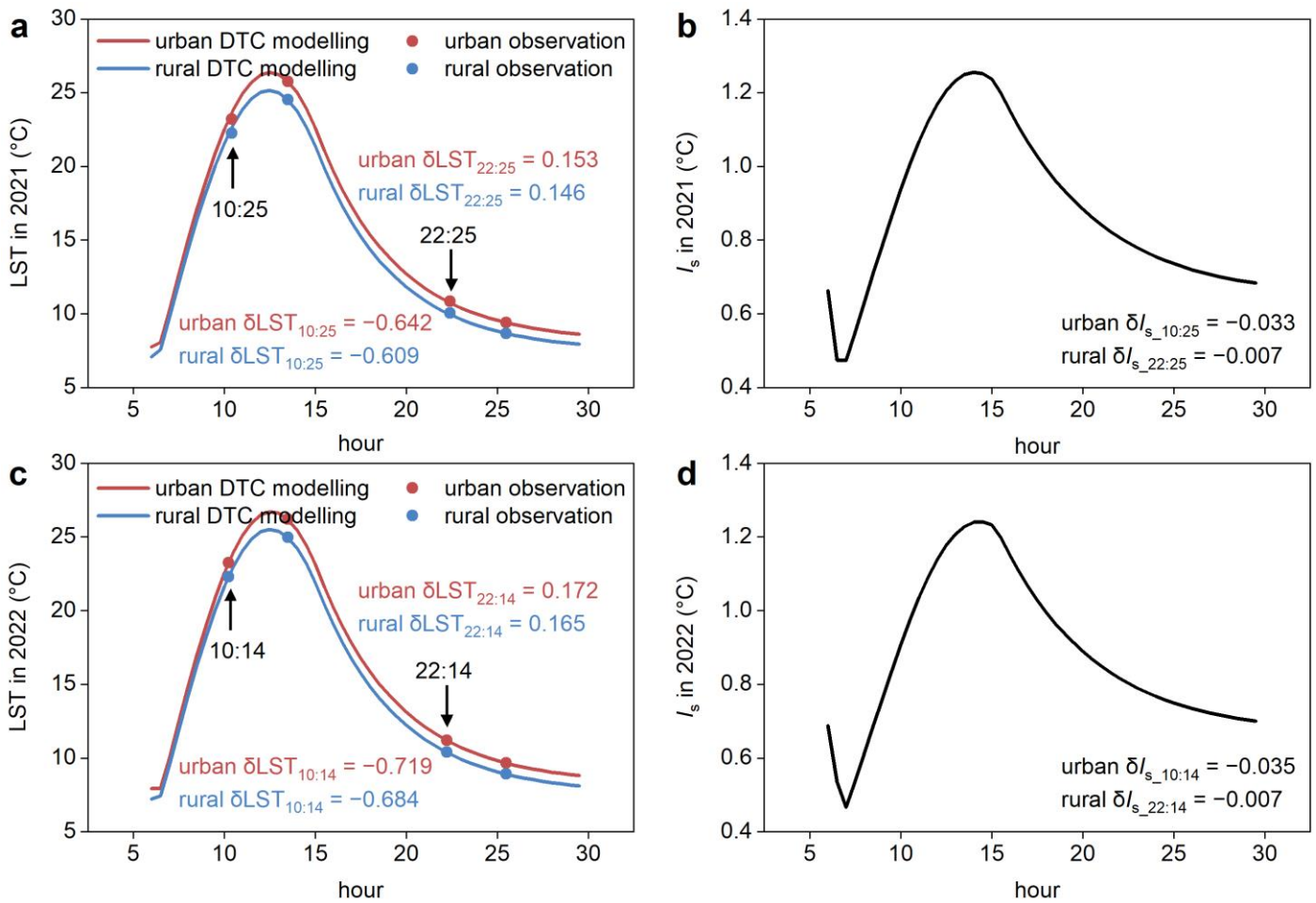


Figure S19. Intra-day modes of urban/rural LST and I_s variations across global 2104 cities based on diurnal temperature circle model. (a) LST mode in 2021; (b) SUHII mode in 2021; (c) LST mode in 2022; and (d) SUHII mode in 2022. δLST (and $\delta SUHII$) denotes the difference of LST (and SUHII) before and after correction for orbital drift. δLST (and δI_s) denotes the difference of LST (and I_s) before and after correction for orbital drift, namely the influence of orbital drift on observed LST (and I_s).

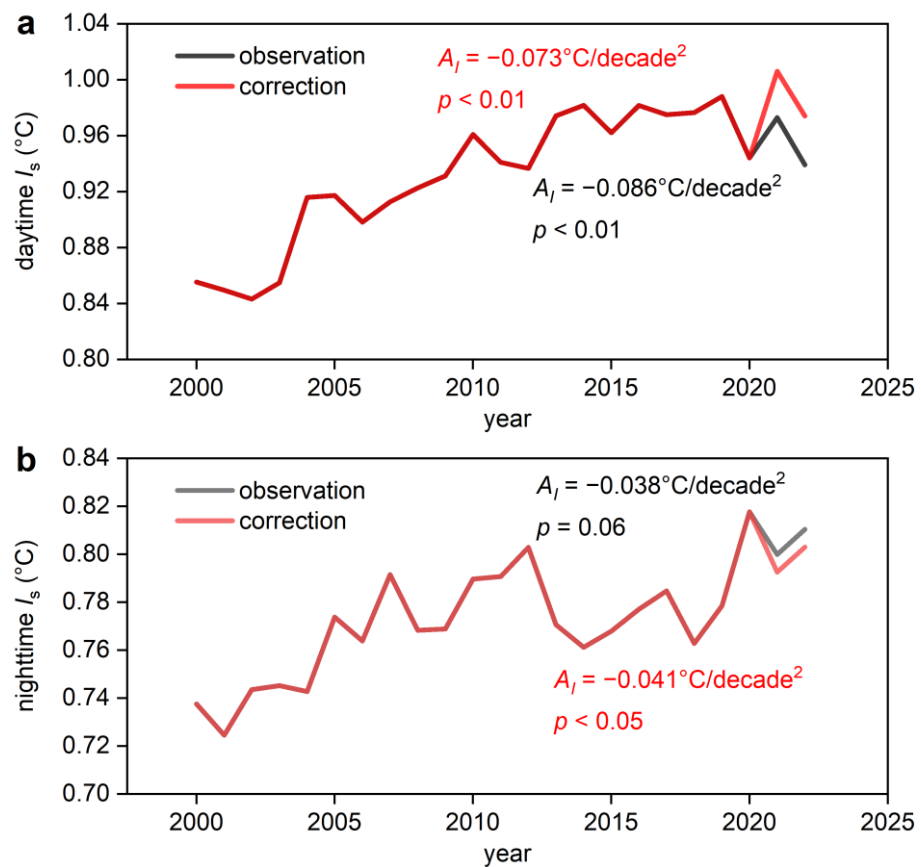


Figure S20. Interannual variations in I_s before (i.e., observation) and after (i.e., correction) correction for orbital drift. (a) Daytime comparison; and (b) nighttime comparison.

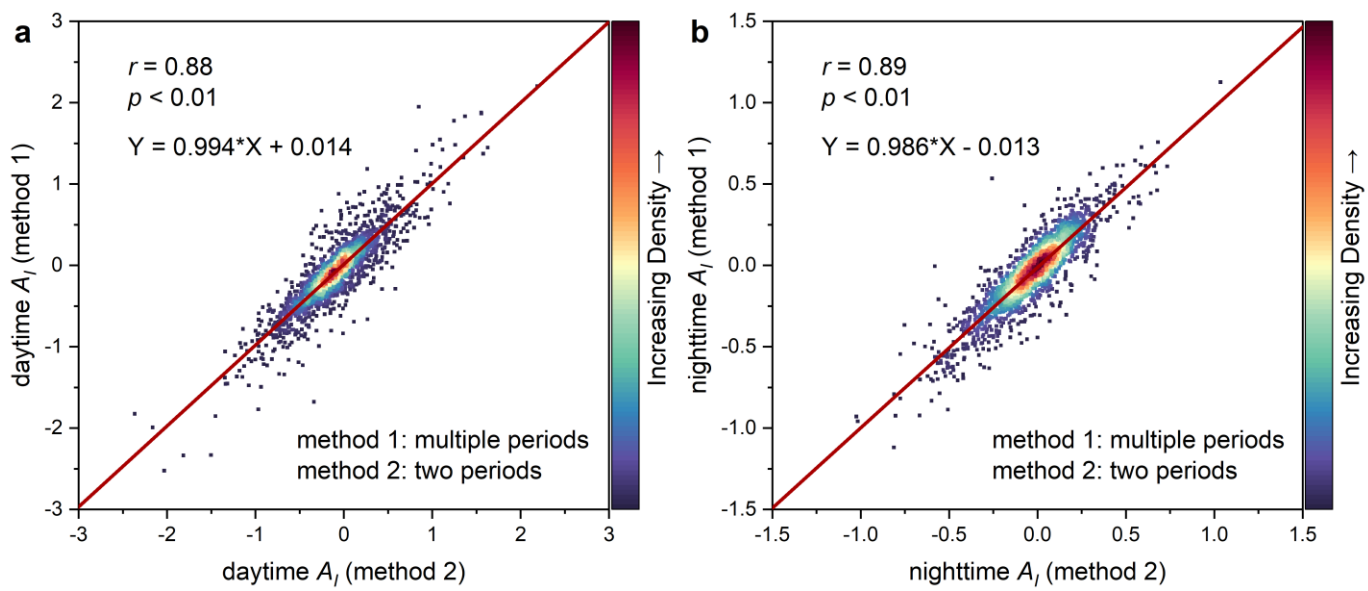


Figure S21. Comparison of A_l estimated by methods based on multiple periods (this study) and two periods (change rate of V_l between 2000-2010 and 2012-2022). (a) Daytime comparison; and (b) nighttime comparison.

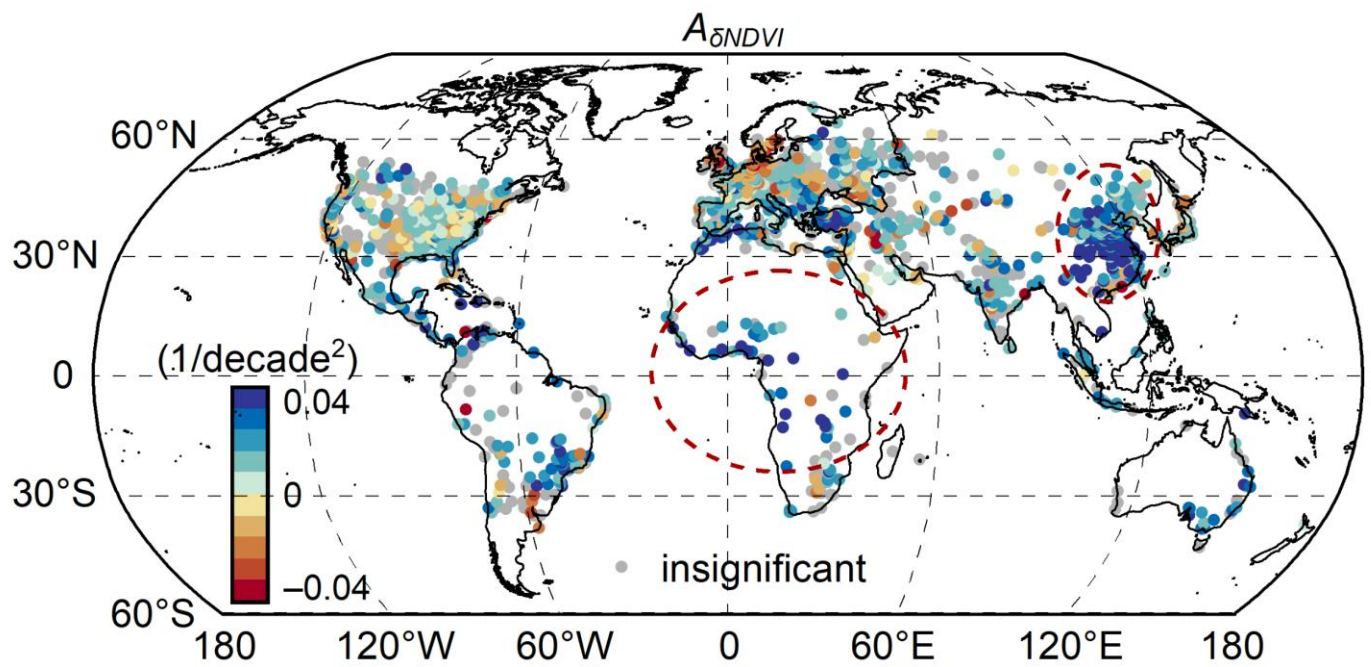


Figure S22. Spatial pattern of the variabilities of the trends of the urban-rural normalized difference vegetation index (NDVI) difference ($A_{\delta NDVI}$) in 2104 cities worldwide for 2000–2022. The red dashed ellipse mainly overlays cities in eastern Asia and Africa with a larger $A_{\delta NDVI}$.

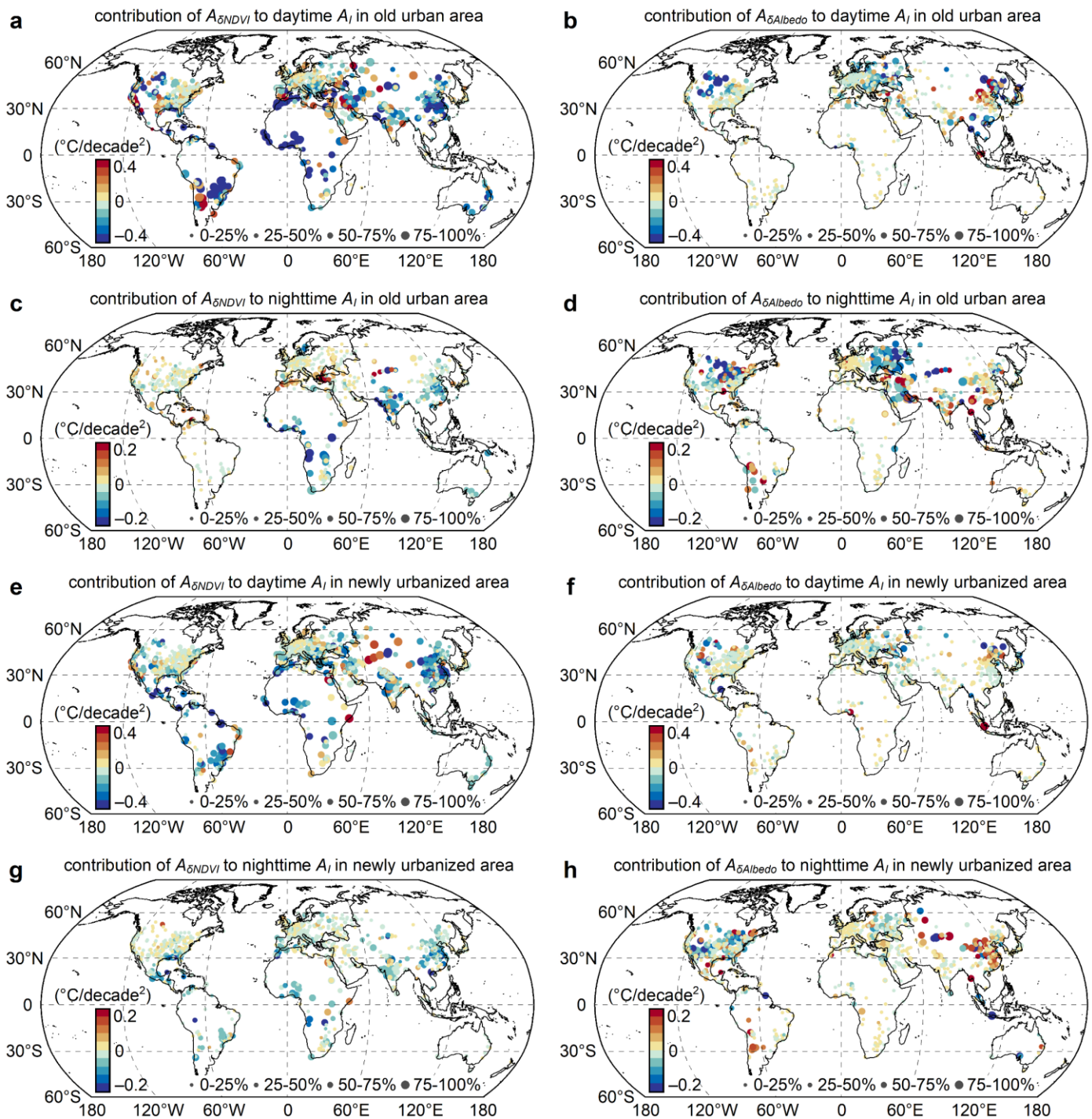


Figure S23. Contributions from the variabilities of the trends of the urban-rural normalized difference vegetation index (NDVI) and albedo differences ($A_{\delta NDVI}$ and $A_{\delta Albedo}$) to the A_i in old urban area and newly urbanized area across global cities. Contributions from the $A_{\delta NDVI}$ (a) and $A_{\delta Albedo}$ (b) to the A_i in old urban area during the day; (c) to (h), as in (a), (b), but showing different cases (e.g., during the day or night, and in old urban area or newly urbanized area). The color and size of the circles signify the value and percentage of contribution from the $A_{\delta NDVI}$ and $A_{\delta Albedo}$ to the A_i .

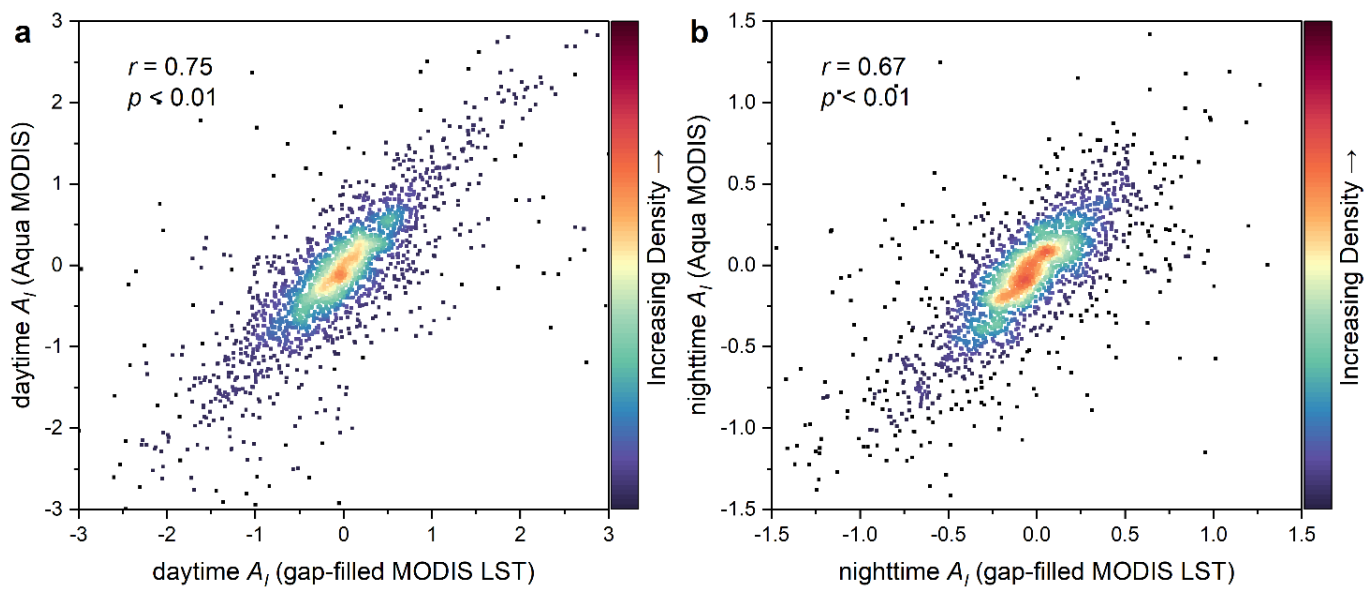


Figure S24. Correlation of A_t estimated by Aqua MODIS LST and gap-filled MODIS LST. (a) Daytime comparison; and (b) nighttime comparison.

C. Supplementary Tables

Table S1. Diagnosis of ordinary least squares (OLS) and geographically weighted regression (GWR) models for describing the relationship between A_i and various drivers.

Variable	Urban		Old urban area		Newly urbanized area	
	Day	Night	Day	Night	Day	Night
OLS diagnostics						
AICc	1378.640146	401.738301	1842.152559	944.974214	1147.243277	146.137117
F-statistic	46.890303	7.158833	40.470028	7.767617	42.698399	9.883292
R^2	0.220428	0.046741	0.200708	0.050570	0.204105	0.062010
R^2 Adjusted	0.215727	0.040212	0.195748	0.044060	0.199325	0.055735
Moran Index	0.166	0.275	0.221	0.256	0.091	0.155
(MI)						
MI Probability	0.000	0.000	0.000	0.000	0.000	0.000
GWR diagnostics						
Neighbors	117	125	110	134	134	126
Residual sum of squares	126.696409	49.289398	187.237825	94.461877	118.823316	40.290729
Effective number	186.090618	144.754918	189.143525	134.452446	164.216233	151.945818
Sigma	0.394059	0.25839	0.488429	0.355475	0.375708	0.231461
AICc	1114.906548	220.326304	1509.788079	773.142331	1003.595237	31.472726
R^2	0.567801	0.41273	0.597448	0.394126	0.478405	0.381604
R^2 Adjusted	0.469756	0.298374	0.500949	0.285966	0.377271	0.257484
Moran Index	0.028	0.023	0.032	0.030	0.023	0.014
(MI)						
MI Probability	0.000	0.000	0.000	0.000	0.000	0.013

Table S2. The regression coefficients (mean \pm one standard deviation) from geographically weighted regression model in describing the relationship between A_i and various drivers.

Drivers	Urban		Old urban area		Newly urbanized area	
	Day	Night	Day	Night	Day	Night
$A_{\delta NDVI}$	-10.28 \pm 5.17	-0.37 \pm 1.75	-11.03 \pm 5.97	-0.27 \pm 2.42	-8.00 \pm 2.83	-1.73 \pm 1.27
$A_{\delta Albedo}$	-9.09 \pm 14.29	-7.78 \pm 8.71	-10.09 \pm 15.08	-7.64 \pm 8.69	-8.52 \pm 12.44	-9.45 \pm 9.93
$A_{\delta AOD}$	0.86 \pm 7.72	2.67 \pm 5.27	-0.25 \pm 6.79	3.22 \pm 4.00	2.12 \pm 7.07	0.04 \pm 5.42
A_{TEMP}	-0.012 \pm 0.055	0.003 \pm 0.044	-0.007 \pm 0.073	0.007 \pm 0.040	-0.024 \pm 0.041	-0.004 \pm 0.042
A_{PRCP}	0.0017 \pm 0.0021	0.0001 \pm 0.0011	0.0023 \pm 0.0024	-0.0001 \pm 0.0015	0.0013 \pm 0.0016	-0.0002 \pm 0.0009
A_{POP}	-0.000019 ± 0.000035	-0.000003 ± 0.000046	0.000010 ± 0.000004	-0.000010 ± 0.000005	-0.000021 ± 0.000033	0.000001 ± 0.000062

D. Supplementary References

- Betts, R. A. (2000). Offset of the potential carbon sink from boreal forestation by decreases in surface albedo. *Nature*, 408, 187–190. <https://doi.org/10.1038/35041545>
- Chakraborty, T., & Lee, X. (2019). A simplified urban-extent algorithm to characterize surface urban heat islands on a global scale and examine vegetation control on their spatiotemporal variability. *International Journal of Applied Earth Observation and Geoinformation*, 74, 269–280. <https://doi.org/10.1016/j.jag.2018.09.015>
- Chakraborty, T., Venter, Z. S., Qian, Y., & Lee, X. (2022). Lower urban humidity moderates outdoor heat stress. *AGU Advances*, 3, e2022AV000729. <https://doi.org/10.1029/2022AV000729>
- Florczyk, A. J., Melchiorri, M., Corbane, C., Schiavina, M., Maffenini, M., Pesaresi, M., et al. (2019). Description of the GHS Urban Centre Database 2015: public release 2019: version 1.0 [Dataset]. <https://doi.org/10.2760/037310>
- Gong, P., Li, X., Wang, J., Bai, Y., Chen, B., Hu, T., et al. (2020). Annual maps of global artificial impervious area (GAIA) between 1985 and 2018. *Remote Sensing of Environment*, 236, 111510. <https://doi.org/10.1016/j.rse.2019.111510>
- Good, E. J., Aldred, F. M., Ghent, D. J., Veal, K. L., & Jimenez, C. (2022). An analysis of the stability and trends in the LST_cci land surface temperature datasets over Europe. *Earth and Space Science*, 9, e2022EA002317. <https://doi.org/10.1029/2022EA002317>
- Gutman, G. G. (1999). On the monitoring of land surface temperatures with the NOAA/AVHRR: removing the effect of satellite orbit drift. *International Journal of Remote Sensing*, 20, 3407–3413. <https://doi.org/10.1080/014311699211435>
- Hong, F., Zhan, W., Götsche, F. M., Lai, J., Liu, Z., Hu, L., et al. (2021). A simple yet robust framework to estimate accurate daily mean land surface temperature from thermal observations of tandem polar orbiters. *Remote Sensing of Environment*, 264, 112612. <https://doi.org/10.1016/j.rse.2021.112612>
- Kottek, M., Grieser, J., Beck, C., Rudolf, B., & Rubel, F. (2006). World map of the Köppen-Geiger climate classification updated. *Meteorologische Zeitschrift*, 15, 259–263. <https://doi.org/10.1127/0941-2948/2006/0130>
- Lee, X., Goulden, M. L., Hollinger, D. Y., Barr, A., Black, T. A., Bohrer, G., et al. (2011). Observed increase in local cooling effect of deforestation at higher latitudes. *Nature*, 479, 384–387. <https://doi.org/10.1038/nature10588>
- Li, L., Zhan, W., Du, H., Lai, J., Wang, C., Fu, H., et al. (2022). Long-Term and Fine-Scale Surface Urban Heat Island Dynamics Revealed by Landsat Data Since the 1980s: A Comparison of Four Megacities in China. *Journal of Geophysical Research: Atmospheres*, 127, e2021JD035598. <https://doi.org/10.1029/2021JD035598>
- Li, X., Gong, P., Zhou, Y., Wang, J., Bai, Y., Chen, B., et al. (2020). Mapping global urban boundaries from the global artificial impervious area (GAIA) data. *Environmental Research Letters*, 15, 094044. <https://doi.org/10.1088/1748-9326/ab9be3>
- Li, X., & Zhou, Y. (2017). Urban mapping using DMSP/OLS stable night-time light: a review. *International Journal of Remote Sensing*, 38, 6030–6046. <https://doi.org/10.1080/01431161.2016.1274451>
- Middel, A., AlKhaleed, S., Schneider, F. A., Hagen, B., Coseo, P., et al. (2021). 50 grades of shade. *Bulletin of the American Meteorological Society*, 102, E1805–E1820. <https://doi.org/10.1175/BAMS-D-20-0193.1>

- Yang, Q., Xu, Y., Wen, D., Hu, T., Chakraborty, T. C., Liu, Y., et al. (2024). Satellite Clear-Sky Observations Overestimate Surface Urban Heat Islands in Humid Cities. *Geophysical Research Letters*, 51, e2023GL106995. <https://doi.org/10.1029/2023GL106995>
- Zhang, T., Zhou, Y., Zhu, Z., Li, X., & Asrar, G. R. (2022). A global seamless 1 km resolution daily land surface temperature dataset (2003–2020). *Earth System Science Data*, 14, 651–664. <https://doi.org/10.5194/essd-14-651-2022>
- Zhao, L., Lee, X., Smith, R. B., & Oleson, K. (2014). Strong contributions of local background climate to urban heat islands. *Nature*, 511, 216–219. <https://doi.org/10.1038/nature13462>
- Zhou, D., Xiao, J., Bonafoni, S., Berger, C., Deilami, K., Zhou, Y., et al. (2019). Satellite remote sensing of surface urban heat islands: Progress, challenges, and perspectives. *Remote Sensing*, 11, 48. <https://doi.org/10.3390/rs11010048>